The Astrophysical Journal, 972:160 (15pp), 2024 September 10
https://doi.org/10.3847/1538-4357/ad5fea

The Contribution of Solar Magnetic Regions to the Residual Meridional and Zonal Flows

D. C. Braun
NorthWest Research Associates, 3380 Mitchell Lane, Boulder, CO 80301, USA; dbraun@nwra.com

Received 2024 May 10; revised 2024 July 3; accepted 2024 July 4; published 2024 September 4

Abstract

We estimate the contributions to the solar-cycle variation of solar meridional and zonal flows near the surface expected solely from local magnetic regions. Maps of flows near magnetic regions are obtained using helioseismic holography and averaged over ensembles of such regions with similar magnetic flux. These averaged flows are assigned to the positions and times of all magnetic regions identified from daily magnetograms over an 11 yr period. Residuals are obtained after averaging both meridional and zonal-flow components over longitude for each Carrington rotation and subtracting the temporal mean at each latitude. Results indicate that magnetic regions produce solar-cycle variations of both components in the active latitude range with peak amplitudes of about 1 m s^{-1}, which represents only a fraction of the known variations in either the residual zonal or meridional flow with amplitudes around 3 and 5 m s^{-1}, respectively. Thus it is unlikely that active regions, and compact magnetic concentrations in general, are the primary source of the 11 yr variation in these global flows. A threshold magnetic flux of 5×10^{20} Mx, below which no significant flows are observed, is identified as a check on the completeness of the set of magnetic regions. We also find that inflows around most magnetic regions are confined to within 10°–12° of their centers, in contrast with recent evidence of more extended inflows.

Unified Astronomy Thesaurus concepts: Solar rotation (1524); Solar meridional circulation (1874); Solar cycle (1487); Solar active regions (1974); Solar active region velocity fields (1976); Solar active region magnetic fields (1975)

1. Introduction

The Sun's axisymmetric, or longitudinally invariant, large-scale flows include both differential rotation and meridional circulation. Both of these global flows exhibit variations with the solar cycle, which, at or near the surface, have comparable magnitudes and spatial patterns that, at least in part, follow the latitude migration of sunspots and other magnetic regions (Howe 2009; Hanasoge 2022). Because of this, these variations are of great interest in understanding the feedback of dynamo-generated magnetic fields onto global flows (Rempel 2006; Beaudoin et al. 2013; Pipin & Kosovichev 2019; Hotta et al. 2023).

The long-term variability of these global flows is typically studied by averaging their meridional or zonal component over the observable longitudes of the Sun for each Carrington rotation (hereafter CR). At each latitude, residuals for each component are obtained by subtracting from the raw values a time average computed over at least one solar cycle. The zonal and meridional residuals of these global flows have currently been recorded over several solar cycles, particularly those representing the photospheric or near-surface values. These include the use of direct Doppler measurements (e.g., Howard & LaBonte 1980), feature-tracking of magnetic or convective features (e.g., Hathaway & Rightmire 2010; Hathaway et al. 2022), and helioseismology of several varieties (e.g., Howe et al. 2005; Komm et al. 2018). Figure 1 shows an example of these residuals obtained using time–distance methods described by Zhao et al. (2014) and applied to Dopplergrams obtained by the Helioseismic and Magnetic Imager (HMI) on board the Solar Dynamics Observatory (SDO; Scherrer et al. 2012; Schou et al. 2012).

The residuals of the zonal flows are also known as the "torsional oscillations" and include alternating bands of slower and faster flows straddling the active latitudes (Howard & LaBonte 1980; Howe et al. 2005; Howe 2009). Amplitudes of these residuals are 3–4 m s^{-1} for latitudes below about 40°. At higher latitudes, and not fully visible in Figure 1, other features visible in the zonal-flow residuals appear to include a poleward propagating branch (Howe 2009). The depth dependence of the torsional oscillation has been probed using global helioseismology with the notable result that at least some components persist throughout most of the convection zone (Vorontsov et al. 2002).

The residuals of the meridional flow also show 11 yr variations, showing bands of flows converging toward the active latitudes (e.g., Chou & Dai 2001; Basu & Antia 2003; Zhao & Kosovichev 2004; González Hernández et al. 2006; Komm et al. 2018; Hathaway et al. 2022). Amplitudes of these residuals are typically around 5 m s^{-1}, which are comparable to the torsional oscillations. Evidence for meridional variations at higher latitudes has been presented but the flow measurements are noisier and more challenging to interpret (Ulrich 2010; Rightmire-Upton et al. 2012; Hathaway et al. 2022). The depth dependence of these residuals, much less of the meridional flow as a whole, is less well understood than their zonal counterparts. At least in part, this reflects the challenges of understanding and removing systematic errors (Hanasoge 2022).

Active region inflows were discovered using local helioseismology methods more than two decades ago (Gizon et al. 2001; Haber et al. 2004; Zhao & Kosovichev 2004). These inflows have peak magnitudes on the order of 10–30 m s^{-1} and extend approximately 10° away from the active region center. Measurements of these relatively weak flows are hampered by the presence of compact (~100 m s^{-1}) supergranular flows,

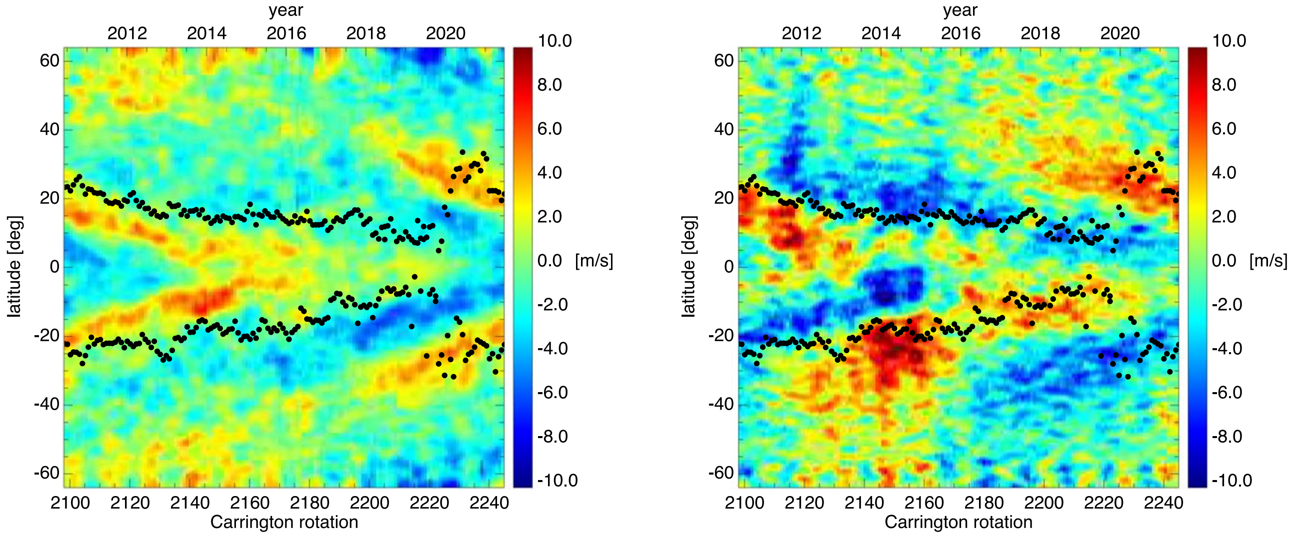

Figure 1. Residuals of the zonal (left) and meridional (right) flows as obtained by Zhao et al. (2014) using the method of time–distance helioseismology applied to Dopplergrams from SDO/HMI over an 11 yr interval starting in 2010 June. The inferred flows shown occur within the first Mm below the surface. The data are available from http://jsoc.stanford.edu/data/timed/. Filled circles indicate the mean latitudes of magnetic regions for each Carrington rotation interval as tabulated in this work.

which act as a source of noise. Ensemble averaging of coaligned flow maps over hundreds or more active regions can substantially reduce this noise (Löptien et al. 2017; Braun 2019; Poulier et al. 2022).

Spruit (2003) suggested active regions provide a possible source of torsional oscillations. The idea is that geostrophic-like inflows could form around active regions due to enhanced radiative cooling, which in the presence of the Coriolis force will produce cyclonic patterns. Flows surrounding active regions are known to have cyclonic vorticity (e.g., Komm et al. 2004; Hindman et al. 2009; Braun 2016), although high-resolution studies of active region flows remain sparse. At any rate, longitudinal averages of flows associated with active regions can plausibly contribute to the solar cycle variations of the zonal and meridional-flow residuals at least within the active latitudes.

To directly assess the role of active region flows in the variation of the meridional circulation, González Hernández et al. (2008) analyzed several years of the near-surface meridional flow during the decline of cycle 23 as obtained from data from the Global Oscillation Network Group (GONG). They found a residual circulation toward active latitudes, which persisted after applying masks that excluded most regions containing surface activity. Moreover, González Hernández et al. (2010) noted changes in the meridional flow during the deep solar minimum concluding cycle 23, which they considered proof that the time-varying features in the meridional flow were independent of surface activity. Using similar helioseismic ring-diagram measurements from GONG, HMI, and the Michelson Doppler Imager (MDI) on board the Solar and Heliospheric Observatory (Scherrer et al. 1995) and spanning more than two solar cycles, Komm et al. (2020) largely confirmed the earlier work of González Hernández et al. (2008). They found amplitudes of the residuals obtained with masks including active regions to be less than one-third larger than using masks excluding such regions.

More recently, several analyses have been carried out using measurements that have higher spatial resolution than those obtained from earlier ring-diagram analyses (Poulier et al. 2022; Mahajan et al. 2023). Using flow maps measured with local correlation tracking (Löptien et al. 2017), Poulier et al. (2022) isolated the active region flows and modeled these to estimate their contribution to the total helioseismic north–south travel-time differences measured using time–distance helioseismology applied to GONG and MDI data (Gizon et al. 2020). They find that inflows associated with active regions account for “only a fraction of the variations” observed in those meridional-flow measurements. Mahajan et al. (2023) applied a series of masks directly to flow maps obtained from the HMI time–distance data analysis pipeline (Zhao et al. 2012). The masks excluded flow contributions at successively greater distances from the positions of active regions, which were identified from the positions of Space-weather HMI active region patches (SHARPs; Bobra et al. 2014). In contrast to earlier studies, Mahajan et al. (2023) concluded that active region inflows extend up to 30° away from their centroids and contribute most of the observed meridional-flow residuals except for features observed at solar minimum between cycles 23 and 24. The latter have a general similarity with the solar minimum flows observed in a solar cycle earlier by González Hernández et al. (2010). Mahajan et al. (2023) also found that the zonal flows are generally not affected by the masking and therefore the torsional oscillation pattern is global in nature. Mahajan et al. (2023) offer several explanations for the difference between their findings and earlier analyses of the meridional residuals, including the possibility that prior analyses may have used masks that do not fully exclude the flows or fail to account for weaker regions.

In this work, we estimate the contribution to both the zonal and meridional-flow residuals, within the top few Mm of the convection zone, due to local magnetic flux concentrations. We take a different approach than some prior studies in that we use high-resolution ensemble averages of flows around magnetic regions (such as those described by Braun 2019) in conjunction with the positions of active regions identified over a solar cycle, to predict the expected residuals in the meridional and zonal flows caused by the active regions alone. An advantage of this approach is that it avoids the use of masks, which, at times near peak solar activity, can become saturated to the point where little or no "quiet" areas remain. The ensembles used to measure the averaged flows can be selected to include regions relatively isolated from one another and therefore allow for reliable assessment and subtraction of the background flows in the nearby quiet Sun.

In Section 2, we discuss the identification of magnetic regions from daily HMI magnetograms. We compare the properties of these magnetic regions with SHARPs to explore further the issues of completeness raised by Mahajan et al. (2023). In Section 3, we construct ensemble averages of flows around magnetic regions. We also carry out new measurements of the spatial extent of active region inflows. Our findings are presented in Section 4, followed by several tests of their reliability in Section 5. The consequences of our findings are discussed in Section 6.

2. Identification of Magnetic Regions

The goal is to tabulate daily lists of the fluxes and positions of magnetic regions that may have local inflows or vortical motion that can contribute to longitudinal averages of global flows. We seek a full accounting of these regions so that estimates of the 11 yr residuals from their associated flows may be directly compared to total residuals (e.g., Figure 1) in order to gauge their effectiveness in causing the variations. The geostrophic-like flows proposed by Spruit (2003) would not seem to require bipolar, or other specific spatial patterns of the photospheric flux to form. Testing these, and other, theories therefore requires some flexibility in defining compact regions of flux that go beyond the historical properties of "active regions" (see van Driel-Gesztelyi & Green 2015). To emphasize this distinction, we use the general term "magnetic region" (or MR) in the following discussion.

This method used here is based on finding the peaks of spatially smoothed magnetograms and is the same used by Braun (2019) and Poulier et al. (2022). The tabulation of MRs is made over a solar cycle, spanning 148 Carrington rotations (CR 2098-2245). To maintain uniformity and continuity of data we selected the first 11 yr of HMI observations, which commenced in early 2010. The interval contains most of cycle 24, which commenced a year prior to the start, and concludes after the first year of cycle 25.

2.1. MR Selection

The surface magnetic field is assessed from the HMI daily "synchronic" magnetogram sampled over the full 11 yr. We use only the 120° longitude segment from these maps that contain the front-side observations obtained daily at noon. We smooth the absolute value of the line-of-sight flux density with a two-dimensional Gaussian function. This operation is performed through a discrete convolution of the flux density with a two-dimensional Gaussian function computed over the spatial grid of the synchronic magnetograms. The grid extends over the longitude and the sine of the latitude with fixed pixel spacings of $0\overset{\circ}{.}10$ and 1.389×10^{-3}, respectively. The FWHM, which we denote λ, is set to 100 pixels in both dimensions. Thus, λ subtends 10° in longitude and latitude at the equator. Local maxima are identified where pixel values exceed the eight neighboring pixels. Starting with the strongest peak, weaker candidates within a distance λ of the stronger one are discarded until there are no more candidates. The total unsigned flux, $\Phi_{\rm box}$, within a $20^\circ \times 10^\circ$ bounding box surrounding each candidate MR was tabulated along with its position. The value of λ was selected by trial and error: setting λ smaller than 10° undesirably divides bipolar MRs into their separate polarities.

To illustrate the regions selected on a typical day, Figure 2 shows MRs identified for 2010 November 21. The date was chosen to represent a day with an average number of identified MRs. The regions are labeled alphabetically in order of decreasing $\Phi_{\rm box}$. The strongest MR candidates *a* and *b* are associated with NOAA numbered regions 11127 and 11126, respectively. The flux-weighted positions of five SHARPs, identified near midday of 2010 November 21, are indicated by blue crosses. Four of these are positioned very close to the strongest four MR candidates *a*–*d*, while a fifth located just to the south of candidate *a* has no MR counterpart. We note that our scheme precludes MRs within 10° of a larger one. The remaining MR candidates (*e* through *m*) present varying appearances and properties. Candidate *g* exhibits an apparent bipolar structure, but most of the others defy a simple classification. Some unipolar regions (e.g., *f*) may represent high-latitude flux remnants of past active regions but many others (e.g., *h* through *m*) appear to be small clusters of ephemeral regions.

We take an empirical approach to defining a threshold flux, $\Phi_{\rm thresh}$, which is required for inclusion in our MR table. Specifically, a threshold of 5×10^{20} Mx was found by measuring ensemble-averaged flows for groups of weak MR candidates and finding the fluxes for which the flow measurements fall below the noise. This is discussed in more detail in Section 3.1. Above this threshold, only the seven candidates *a* through *g* (boxes outlined in solid lines) are included for this particular day in our final MR tables, while weaker regions (boxes outlined in dotted lines) are excluded. In general, this threshold appears to exclude most short-lived features including clumps of ephemeral regions while leaving others, such as candidate *f*, which mostly occur at relatively high latitudes and may represent remnant flux from past active regions.

2.2. MR Properties

The flux distribution of the complete set of MR candidates is shown in Figure 3. The distribution of SHARPs is also shown. To facilitate a consistent comparison, we use only SHARPs present at 12 UT on each day and we measure $\Phi_{\rm box}$ for these regions from the HMI synchronic magnetogram in the same manner as the MR candidates. It is emphasized that there are significant differences between the flux $\Phi_{\rm box}$ and the value of the keyword USFLUX as stored in the SHARP metadata. We discuss this further in the Appendix, but we note that the discrepancy results largely due to the varying bounding box over which USFLUX is assessed.

We obtained 70,498 total MR candidates, counted daily, over the 11 yr interval, with 28,059 MRs above the flux threshold. For comparison, there are 20,128 daily SHARPs over the same time interval and 120° longitude range. The patches defining SHARPs can span multiple NOAA regions (Bobra et al. 2014) but in other instances can form tight pairs or clusters as shown in Figure 2. SHARPs are identified using substantially different criteria, including considerations based on their morphology and temporal evolution, than simply finding local maxima in flux. Consequently, differences in their distribution, as shown in Figure 3, are expected. However,

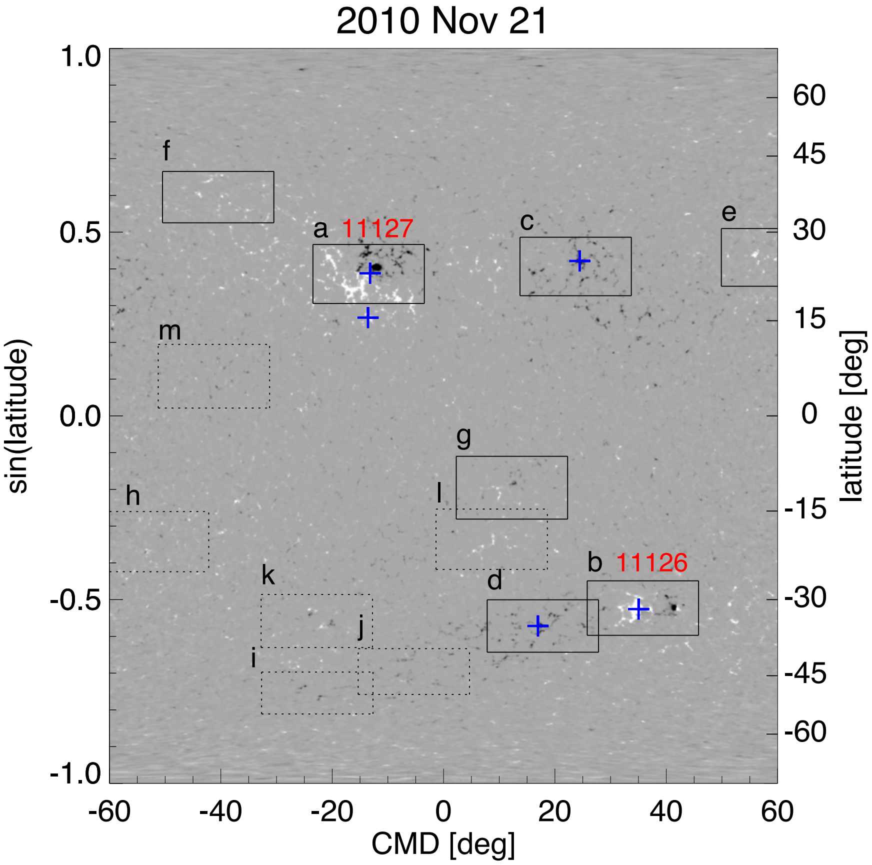

Figure 2. A portion of the HMI synchronic magnetogram for 2010 November 21, showing only the longitudes within 60° of the central meridian. Bounding boxes spanning 20° in longitude and 10° in latitude surround all magnetic regions identified using the method described in Section 2.1. The MRs are alphabetically labeled in order of decreasing flux as measured within the boxes. The seven strongest regions (a–g) above a threshold flux are indicated by solid boxes and included on this day in the estimate of the residual flows. The weaker regions (h–l), indicated by dotted boxes, are not included. Two regions are labeled with their NOAA designation assigned to the visible spot groups. Blue crosses are placed at the location of five SHARP members.

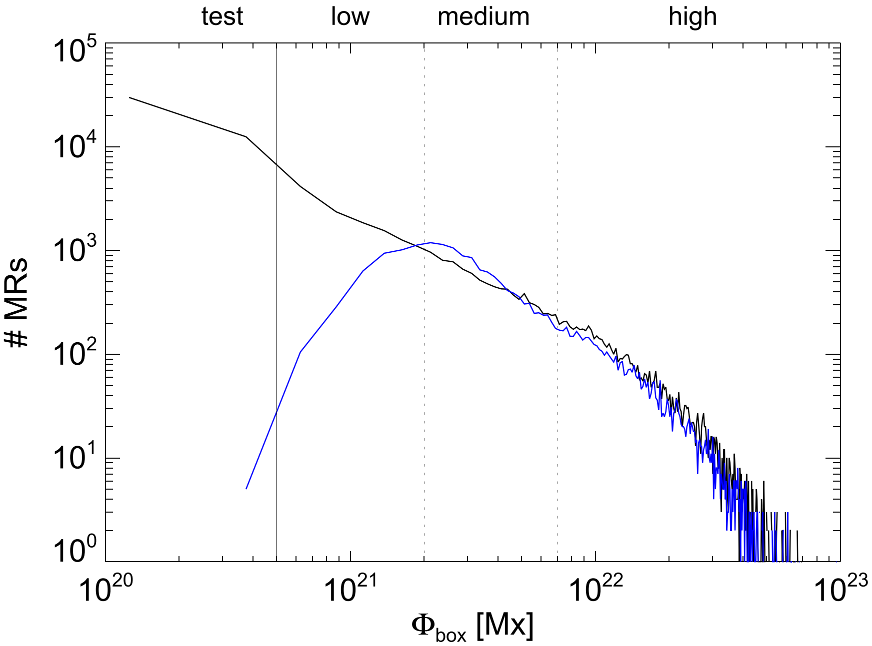

Figure 3. Distributions in the flux of the sample of magnetic regions (black line) identified using the method described in Section 2.1 and applied to an 11 yr interval of HMI synchronic magnetograms. The blue line shows the distribution of SHARP regions for the same interval. The magnetic flux is determined in the same manner for both sets of regions (see text). The solid vertical line indicates the threshold flux $\Phi_{\rm thresh}$ while the two dotted vertical lines represent boundaries between the three main flux groups.

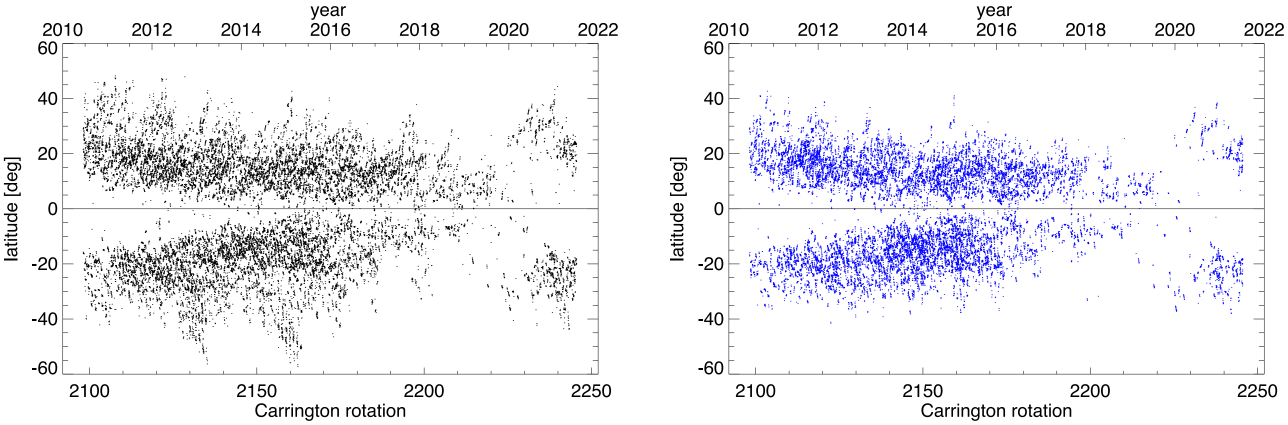

Figure 4. Times and latitude (left panel) of magnetic regions over the 11 yr as identified from daily HMI magnetograms using the procedure discussed in Section 2.1. The right panel shows the same for a set of SHARP members. The top scale shows the date while the bottom scale indicates the Carrington rotation number.

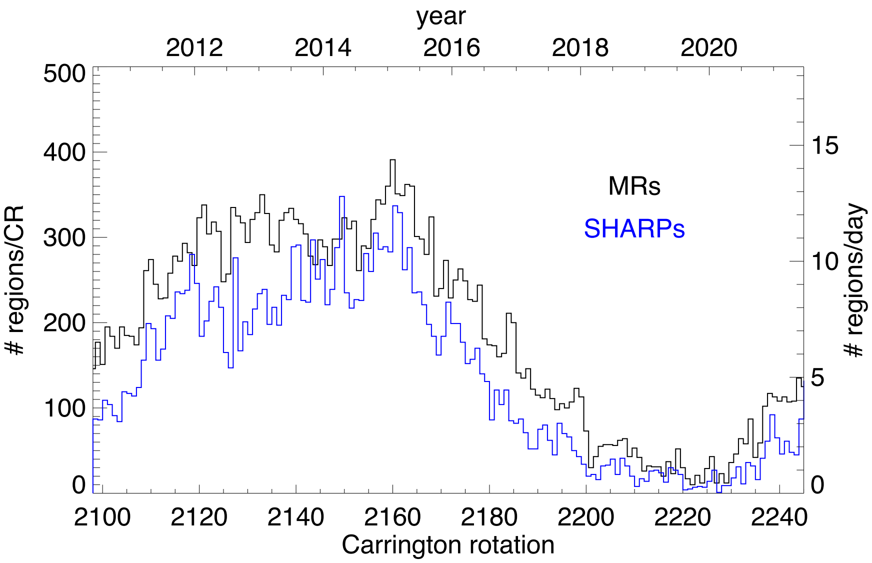

Figure 5. Number of magnetic regions identified in each Carrington rotation. The black line indicates the regions identified in this study while the blue line shows the number of SHARPs, as counted daily, for the same rotations. The scale on the right shows the mean daily count over each rotation assuming a 27.3 day rotation period.

there is a remarkable similarity between the flux distribution of MRs and SHARP regions except for fluxes below about 10^{21} Mx where they diverge substantially. A detailed comparison of the two sets reveals that approximately 90% of the SHARPs spatially coincide closer than 10° with one or more of our MRs. However, only about 60% of the MRs match one or more SHARP regions. The bulk of the nonmatching MRs occur at the lowest fluxes. We examine in more detail the sensitivity of the calculations to the details of the MR selection, including differences between our MRs and SHARP regions, in Section 5.

Figure 4 shows the distribution in time and latitude of our MRs as well as the SHARPs for comparison. Both distributions are similar in general, although there appears to be an excess of MRs at higher latitudes. Many of these high-latitude MRs persist for several rotations and appear to represent flux remnants of active regions, as exemplified by the MR labeled *f* in Figure 2.

Counts of MRs (and SHARPs) for each Carrington rotation are shown in Figure 5. Both distributions show a strong solar cycle variation. It is noteworthy that rejected MR candidates, with $\Phi_{\rm box} < \Phi_{\rm thresh}$, exhibit considerably less latitude and time variability. For example, these MR candidates are more (or less) prominent at the cycle minimum (maximum) and thus occur more evenly over the cycle. They are also more spread out over latitude, although weaker concentrations at active latitudes are still apparent. This appears to be consistent with an identification of such regions with clusters of ephemeral regions, which occur mostly by happenstance. Ephemeral regions are known to exhibit much smoother distributions in latitude and time (Harvey et al. 1975; Martin & Harvey 1979).

3. Ensemble-averaged Flows

Maps of the flows are obtained using the "calibrated-holography" method (Braun 2019). Briefly, this employs a lateral-vantage (or deep-focus) geometry (e.g., Lindsey & Braun 2004) with a focus depth of 3 Mm below the photosphere. The result is a map of travel-time differences of waves propagating between opposite quadrants of an annular pupil. As was carried out in prior analyses (Braun 2016, 2019), a numerical calibration is used to convert these travel-time differences to components of flow. Initially derived using Postel projections from full-disk HMI Dopplergrams, these

Table 1
Properties of Flow-survey Sample

Group	$\Phi_{\rm box}$ Range (10^{21} Mx)	T_{30} (days)	T_{60} (days)	$T_{\rm samp}$ (days)	med($\Phi_{\rm box,samp}$) (10^{21} Mx)	$T_{\rm mr}$ (days)	med($\Phi_{\rm box,mr}$) (10^{21} Mx)
Test	0.2–0.5	481	407	888	0.36	20,245	0.27
Low	0.5–2.0	593.8	470.0	1063.8	1.1	12,276	1.0
Medium	2.0–7.0	599.5	493.5	1093.0	3.6	9,067	3.6
High	>7.0	1058.0	313.0	1372.0	14.7	6,717	11.3

flows are transformed into their latitude and longitude components.

In Section 3.1 we describe the selection of our MR ensembles consisting of both existing (Braun 2016, 2019) and new flow measurements. Ensemble averages of the flows are described in Section 3.2, which also includes a justification of the flux threshold imposed and a discussion of the subtraction of background flows. In Section 3.3 we use the ensemble-averaged flows to derive the spatial extent of the observed inflows. This is motivated by new observations (Mahajan et al. 2023), which imply more spatially extended inflows than previously suspected.

3.1. Flow Sample

The sample of flow measurements consists entirely of MRs in cycle 23 spanning the years 2010–2019. It is important that the flow measurements selected are representative of all MRs present over the interval, particularly in having a similar distribution in flux. We make use of existing flow maps, described by Braun (2019), and make additional flow measurements in order to adequately cover the full range of MR fluxes present in the 11 yr interval. Some existing flow maps (Braun 2016) were centered on tabulated positions of the strongest NOAA active regions. To maintain uniform selection criteria for all samples, these prior flow maps were only used if they were located within 3° of a region identified using the method described in Section 2.1. The regions studied in our prior surveys (Braun 2016, 2019) were tracked at the Carrington rotation rate over time intervals of 13.65 hr. These maps span 30° in longitude and latitude with a pixel spacing of 0°.0573. Flow measurements for additional regions used in this study were also obtained and fall into two categories. The first consisted of flow maps with identical parameters to the prior maps while the second group covered a larger 60° × 60° region. These larger flow maps provide the basis for the discussion of the spatial extent of the MR flows (Section 3.3) and were obtained from 12 hr intervals of Dopplergram data.

All selected flow maps are constructed from Dopplergrams time series with at least 70% duty cycle and are centered within 60° of the disk center at the midpoint of the observing interval. We divide the distribution of MR fluxes into four groups. The first group ("test") consists, for demonstration purposes, of a selected group of MR candidates with $\Phi_{\rm box} < \Phi_{\rm thresh}$ The MRs selected above the flux threshold are split between three, similarly sized, groups labeled "low," "medium," and "high." To allow the comparison between the MR measurement sample and the total sample, Table 1 shows the combined duration of the measurements for each of the groups, which are defined by the range in $\Phi_{\rm box}$ as specified. The total duration of flow observations, in units of days, consists of the sum of individual flow-measurement intervals (either 12 or 13.65 hr) over all the MRs in the flux range. The quantities T_{30} and T_{60} refer to the duration of the flow maps spanning 30° × 30° and 60° × 60°, respectively. The sum of these, $T_{\rm samp}$, can be directly compared with the number of daily counts of all MRs, $T_{\rm mr}$, in the same flux range over the 11 yr interval. For example, the 1093 days of MR flow measurements selected for the medium-flux group represent about 12% of the entirety (9067) of the MR sample with this flux.

Figure 6 shows the distribution in flux of the measurements, for the three groups above the threshold, as compared with the flux distribution of all MRs over the 11 yr interval. The two curves represent the duration of available measurements (orange), and the number of daily counted MRs (black), for each flux bin. They can be directly compared as both are counted in units of days. The median fluxes of the flow subsample, med($\Phi_{\rm box,samp}$), and complete MR list, med($\Phi_{\rm box,mr}$), are listed in Table 1 and indicated by fiducial marks in Figure 6. As Figure 6 illustrates, the subsample of MRs for which flows were obtained is representative of the complete set of MRs present. The median values of the complete MR set for each flux group are reasonably matched in the measurement samples.

3.2. Averaged Flows

Ensemble averages of the flow components for each of the four flux groups were made. These flow maps were aligned, before averaging, to the centroid positions derived from unsigned HMI magnetograms obtained near the midpoints of the measurement interval. The remapping to the centroid position was performed on each flow component using bicubic interpolation and magnetic regions in the southern hemisphere are flipped vertically. The ensemble-averaged flows are thus defined in terms of longitude and latitude offsets (ΔL, ΔB) from the common centroid position. ΔL is negative (positive) toward the east (west) directions while ΔB is negative (positive) toward the equator (poles).

The background flows present in the quiet Sun, including differential rotation and meridional flow, are assessed and subtracted from the ensemble-averaged flow components using a procedure similar to that employed by Braun (2019). This consists of fitting a cubic polynomial in latitude to the average of two vertical strips of the flow maps situated at longitude offsets of $\Delta L = \pm 13°$. Figure 7 shows an example of this for the "medium" flux ensemble. The quiet-Sun longitude offsets are justified in Section 3.3.

Figure 8 shows the corrected MR flow components, obtained by subtracting the quiet-Sun fits, averaged over the four flux groups considered. These corrected components thus represent flows measured with respect to the nearby quiet Sun at the same latitude. Also shown is the signed flux density from the ensemble averages using line-of-sight magnetograms. The results for our three flux groups resemble those presented by Braun (2019), albeit using somewhat different flux ranges. The

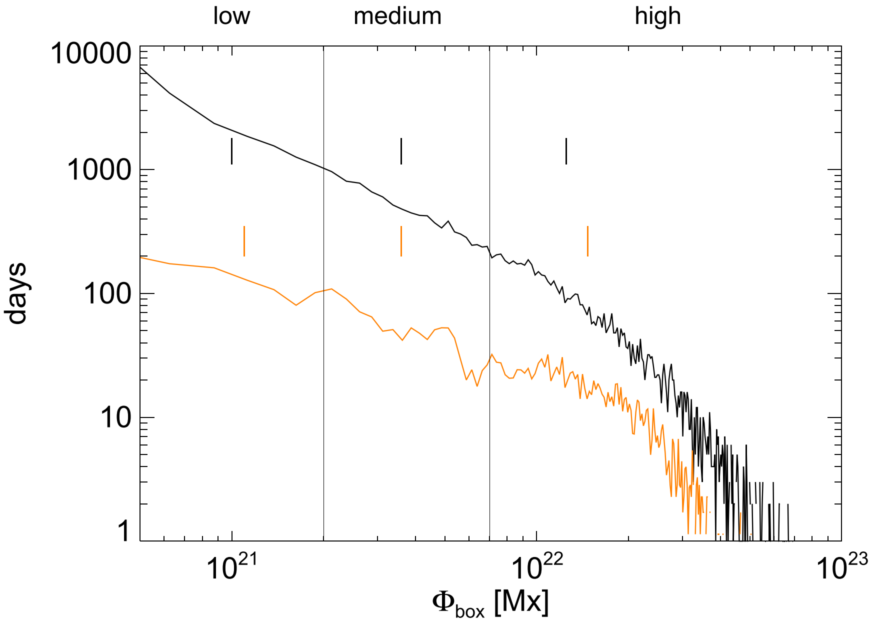

Figure 6. Distribution of the flow measurements (orange line) with flux is compared with the distribution of all magnetic regions over the 11 yr interval (black line). To facilitate this comparison, the counts on the ordinate are expressed in days, with the orange line indicating the total duration of the observations made and the black line indicating the total number of magnetic regions counted daily. Vertical fiducials in either color indicate the median flux for the appropriate population as obtained over the three flux regimes "low," "medium," and "high."

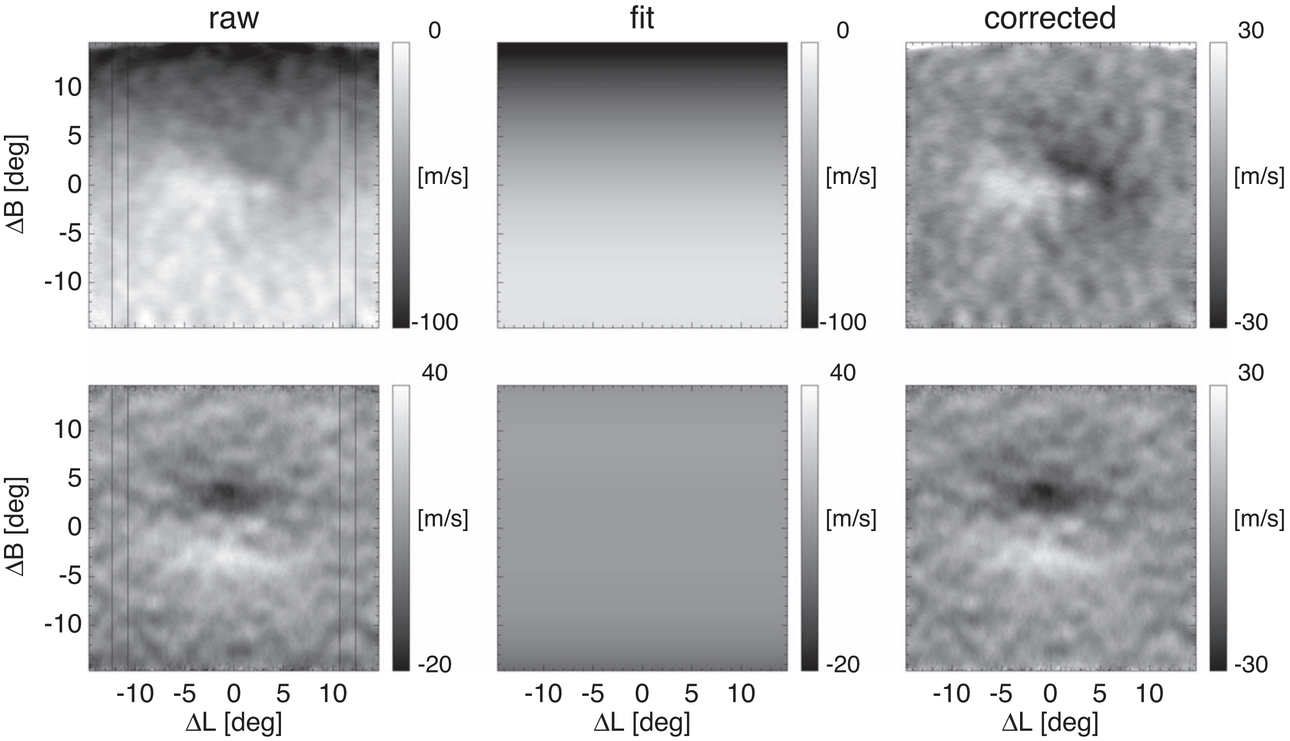

Figure 7. Coaligned averages of the zonal (top row) and meridional (bottom row) flow components over the medium-flux ensemble. The axes represent longitude and latitude offsets from the center of the frame. The left columns show the raw averages, with the two sets of vertical lines indicating the region over which the background flows are fit as a function of the latitude. The middle column shows the results of the fitting while the right panel shows the corrected flows after subtracting the fits from the raw components. The speeds shown in the raw and background-fit frames are with respect to a fixed Carrington rate, at which all of the HMI Dopplergrams were tracked. The corrected flows are thus relative to the nearby quiet Sun at each latitude.

results for the "test" group show little or no significant flow signatures. Of primary interest for estimating the local MR contributions to global flows is the average of the flow components over longitude, which is shown in Figure 9.

The longitudinal average of the "test" flow components shown in Figure 9 is consistent with zero. This justifies the flux threshold used in the MR identification. Some general properties of the flows in our remaining three MR flux groups shown in Figures 8 and 9 are worth noting. First, the meridional-flow profiles (shown in the left panel of Figure 9) are antisymmetric with respect to ΔB and are consistent with an inflow toward the center. The inflow speeds generally increase with flux. As

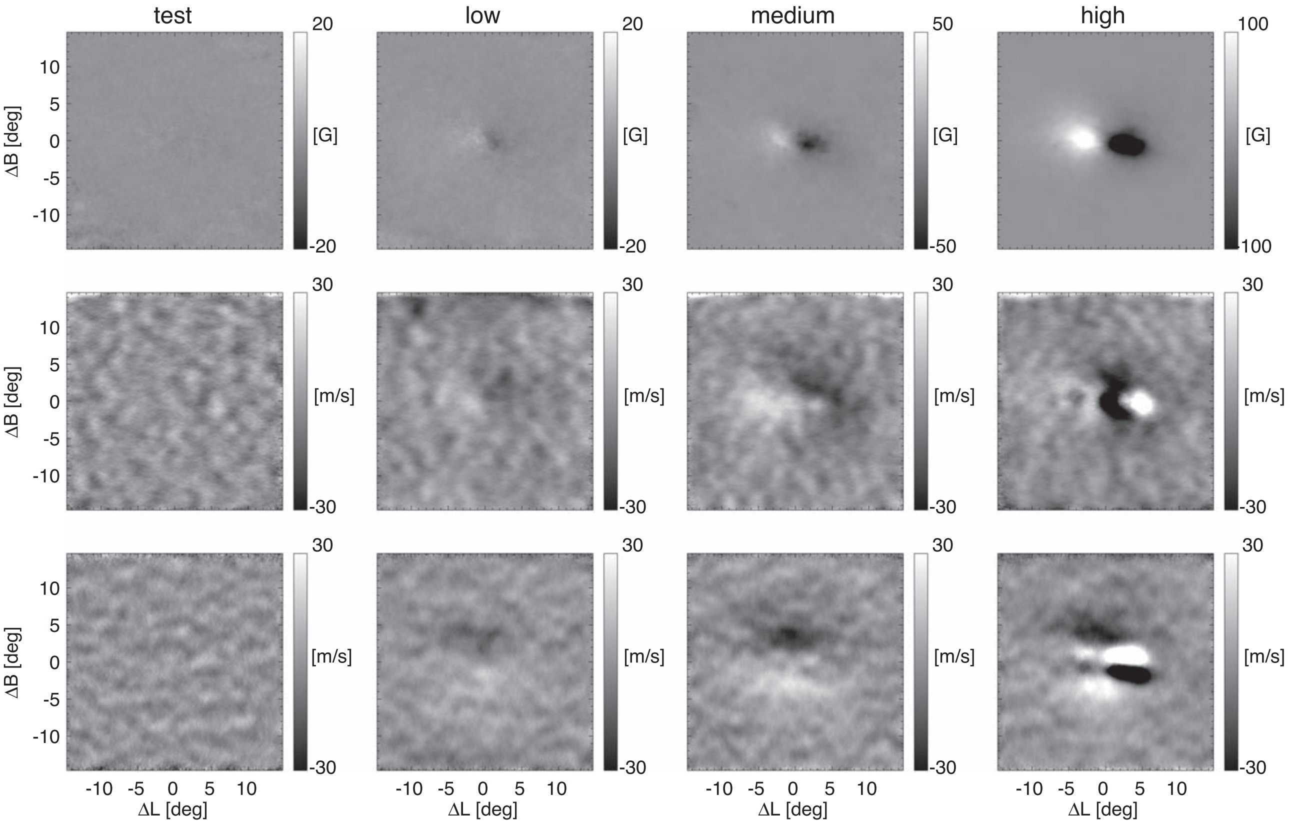

Figure 8. Ensemble averages of the signed magnetic flux density (top row) and the corrected zonal (middle row) and meridional (bottom row) flow components. Results are shown for the four flux groups as labeled at the top of each column. Note that the range in flux density (grayscale) varies from the weaker to the stronger flux groups.

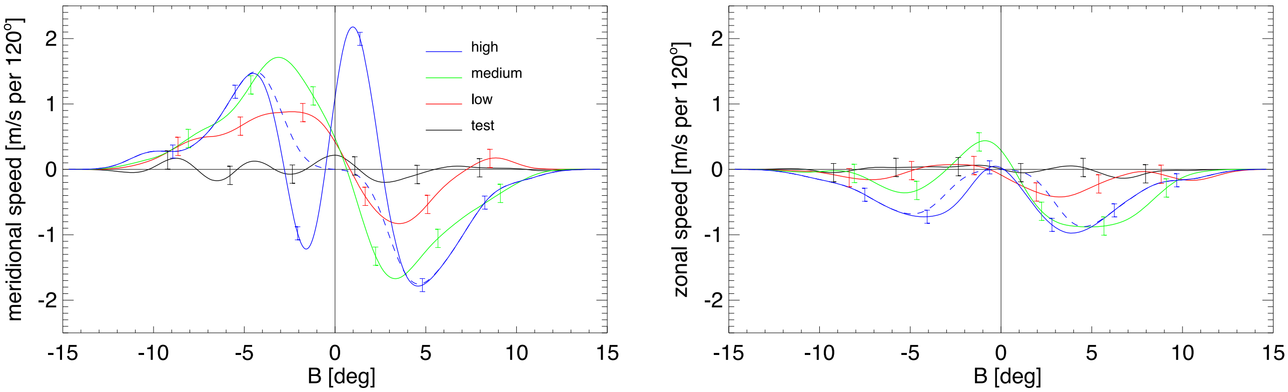

Figure 9. Average over longitude of the corrected flows shown in Figure 8, showing (left panel) the meridional and (right panel) the zonal speed. The speed is relative to fits to the nearby quiet Sun and is scaled so as to represent an average speed over a 120° range of longitude. Averaged flow profiles for the four flux ensembles are indicated by the solid lines with colors as labeled. The dashed blue line indicates a modification of the highest-flux group (blue) profile, which omits the sunspot moats (see text). Only a handful of representative 1σ error bars (denoting the error of the mean over longitude) are shown for clarity.

noted in an earlier study (Braun 2019), the contribution of sunspot moats, exclusive to the high-flux group in our current study, complicates the appearance of the ensemble-averaged flows. The outflows in these moats give rise to strong dipole-like features in the high-flux group. In the high-flux column of Figure 8, these dipoles are oriented horizontally in the zonal contribution and vertically in the meridional contribution. The longitudinal average of the meridional-flow component for the high-flux group (blue curve) in the left panel of Figure 9 shows this outflow as a strong compact sinusoidal signal with a reversed sign from the more latitudinally extended MR inflow signal. The moats contribute much less to the longitudinal average of the zonal components (right panel), due in large part to their symmetry. Considering their predominance in Figure 8 and, noting possible complications and systematics of measuring flows near strong sunspots, we constructed versions (shown by the dashed blue curves) of the high-flux flow profiles without the moats. This is more fully described in Section 5. The zonal-flow profiles (right panel of Figure 9) are dominated by prominent peaks of retrograde (with respect to nearby quiet Sun) motion flanking both the poleward and equatorward sides of the MRs. These retrograde flows are generally stronger on

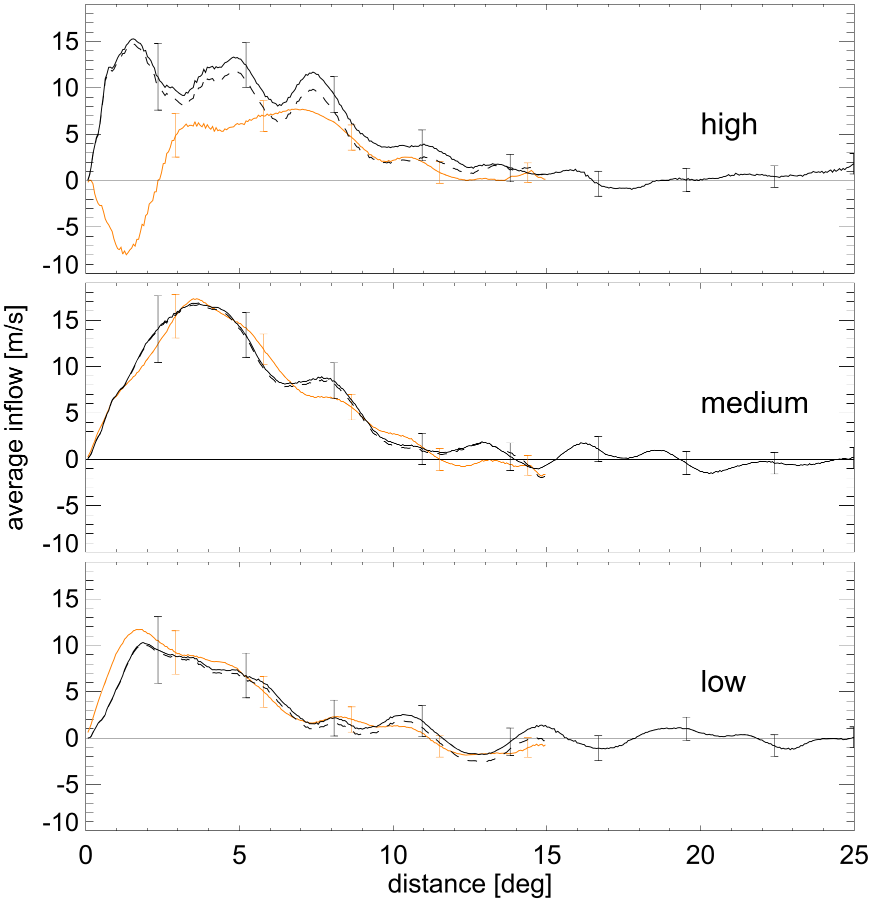

Figure 10. Flows toward magnetic regions, averaged azimuthally, as a function of the distance from the region center. Inflows are positive while outflows are negative. The three panels show results for the three flux groups considered in this study as labeled. The two black lines distinguish between flows using different assessments of the quiet-Sun background, using the subset of flow measurements spanning 60° × 60°. Solid (dashed) lines represent flows obtained from fits to the quiet Sun at ±13° (the nominal case) and ±25° (see text). For comparison, the results in orange represent measurements from the full ensemble as employed in this study. For the most part, there is general agreement with the three inflow measurements for each flux group. An exception is the high-flux group for which measurements within about 3° are affected by the occurrence of strong sunspot moats.

the poleward side of the MRs. The general properties of ensemble-averaged flows near active regions are discussed more fully in Braun (2019).

The error bars shown are derived from the variance of the profiles between subsamples of the ensemble. Each ensemble-averaged flow profile was also checked for possible systematic differences between samples selected for specific spatial properties. This included dividing each sample based on location in the northern or southern hemisphere, and also based on the center-to-limb distance of the MRs. No statistically significant differences, i.e., greater than the formal errors, were found in these comparisons.

3.3. Spatial Extent of Inflows

The flow signatures illustrated in Figures 8 and 9 are fairly compact visually and confined to within about 10° of the center. We note that this is consistent, at least qualitatively, with other assessments of inflows toward magnetic regions (Braun & Wan 2011; Löptien et al. 2017; Braun 2019; Poulier et al. 2022) Recently, Mahajan et al. (2023) carried out an analysis of helioseismic time–distance HMI-based data and inferred inflows extending up to 30° from magnetic regions. The inference is based on comparing measurements of the longitudinal-and-time average of meridional and zonal flows after applying circular magnetic region masks. As noted by Mahajan et al. (2023), one implication of this is that the methodology used to obtain and subtract quiet-Sun flows (e.g., as discussed in Section 3.2) may be compromised by contamination of these extended flows into regions assumed incorrectly to be “quiet.”

To directly test this possibility, we measure the spatial extent of inflows observed with the ensemble averages of the three magnetic flux groups using different determinations of the quiet-Sun background. Making use of the subset of MR flow observations spanning 60° × 60° (see Section 3.1), we assess the background flows using quiet-Sun offsets of $\Delta L = \pm 13°$ as well as ±25°. After subtracting the background, the corrected flows are compared to assess the sensitivity of the results to the choice of the quiet-Sun offset. For determining the inflow speed, the latitude and longitude components of the averaged flows are remapped to a Postel projection with a tangent point set to a typical MR latitude of 20° (the results are not highly sensitive to this choice). We assess a radial inflow component of the surface flow, which is the projection of the flow along a great circle intersecting the MR center. The radial inflow is averaged over the azimuth angle to obtain the inflow as a function of the distance from the region center. Figure 10 shows the resulting azimuthally averaged inflow speeds, for each flux group. Measurements after removal of the nominal $(\Delta L = \pm 13°)$ and more extended $(\Delta L = \pm 25°)$ quiet-Sun backgrounds are shown by the solid and dashed black lines, respectively. There is little significant difference within the formal errors between the inflow speeds as measured with quiet-Sun offsets of either 13° or 25°. For both cases, the inflows are confined to approximately 12°. The good agreement provides confidence that our choice of the nominal quiet-Sun offset is reasonable. The inflow speeds determined for the whole ensemble, and corrected with the nominal background, are shown in orange for context. The agreement between the orange curves and the black ones indicates that, for the most part, the subsample of MRs spanning $60° \times 60°$ is representative of the complete sample. The exception to this is the behavior of the inflows observed near the centers of the highest-flux regions, for which there are significant deviations between the orange and black curves. While essentially all sunspots have moats, their existence and precise location (to within a few degrees) with respect to the MR flux-weighted center varies from region to region. Inflow measurements near the location of sunspots can vary substantially between different MR samples, due to having small sample sizes, for example. This does not detract from the purpose or the results of the comparisons, which are focused on the MR inflows at greater distances.

4. Contribution to Global Meridional-flow and Zonal-flow Residuals

Assuming that all magnetic regions as tabulated in Section 2 have flow fields typical of the representative ensemble averages shown in Section 3 it is straightforward to estimate the contribution of MRs to the global, longitude-averaged, meridional, and zonal flows. We divide the 11 yr time series into individual Carrington rotations each containing a whole number of days, rounding the start and end times of each rotation interval to midnight. Looping through the tabulated list of MRs observed on each day, the zonal- and meridional-flow profiles shown in Figure 9 are shifted in latitude and added together. These daily meridional and zonal sums are then averaged over each 27 (or 28) day interval. At each latitude, the mean over the entire 148-rotation (11 yr) interval is then subtracted to provide MR-contributed residuals, which can be directly compared to the total residuals of the global flows (e.g., Figure 1). Figures 11 and 12 show the resulting meridional and zonal residuals, respectively.

To quantify the temporal variations at each latitude, the residuals are fit to a sine function $f(t) = a\sin(2\pi[t - t_0]/T + \phi)$, where t is time, t_0 is the start of the interval and $T = 11$ yr. Figures 11(c) and 12(c) show examples of these fits. The same fitting is done to the total HMI time–distance residuals shown in Figure 1. The amplitude a and phase ϕ as functions of the latitudes are shown in Figure 13. The meridional-flow residuals due to MRs (Figure 11) resemble, at least superficially, the total residuals (Figure 1). Both the total and MR-contributed variations in meridional circulation appear as converging zones centered on the mean latitude of the MRs. However, it is clear that the amplitude of the variations due to MRs is substantially less than the total observed amplitudes (top left panel of Figure 13). Moreover, the latitudes that exhibit the greatest total residual amplitudes occur around 30° while the MR contributions peak closer to 10° from the equator. That being said, there is better, but not perfect, agreement between the phase of the MR contributions and the total (bottom left panel).

The MR contributions to zonal-flow variations also fall far short of the total zonal residuals (torsional oscillations). Moreover, there is poor agreement between the phase of the MR contributions to the zonal flows and the total phase. The sense is that the MR contributions to the zonal flows show significantly smaller amounts of latitudinal variation (or shear) than is exhibited in the torsional oscillation as a whole. This is readily apparent in Figure 12, where the zonal residuals are dominated by retrograde motions associated with the MRs. These retrograde flows flank individual MRs, primarily on the poleward side, as illustrated by the flow profiles shown in the right panel of Figure 9.

It is also noteworthy that 11 yr variations in the residual flows of both components exist to latitudes higher ±40°, while the MR contributions essentially disappear. As one might expect, the amplitude of the MR contribution roughly follows the latitude distribution of the regions themselves, while it is clear the total residuals persist to at least ±60°.

5. Tests of Methodology

We carried out several modifications of the calculations to test the sensitivity of the results to uncertainties in the measurements and analysis. First, we estimated the contributions to meridional and zonal residuals after removing all flows within ±3° of the magnetic region center. It is suspected (Braun 2019) that magnetic artifacts may compromise (i.e., produce spurious) flow measurements in the vicinity of strong flux and, in particular, sunspots. As revealed with tests carried out with artificial data provided by MHD simulations, the bulk of this anomaly appears confined to the sunspot moats, where measurements may differ from the true values by a factor of 2 or so (see Appendix A of Braun 2019). To test the sensitivity of our results to uncertainties in the moat regions, we employ the modified flow profiles for the highest-flux group, which are shown by the dashed blue curves in Figure 9. This modification consists of masking out both meridional and zonal components of the ensemble averages, for ΔB between $-3°$ and $+3°$, before smoothing the profiles. Figure 14 shows the amplitude and phase of the resulting variation in residual flows. There is essentially no significant difference between the predicted contributions with or without the moat regions. Thus we have some confidence that our results are robust with respect to possible measurement anomalies within 3° of sunspots.

Second, we estimate the MR contributions using tabulated SHARP positions instead of our MR tables compiled and discussed in Section 2. This is motivated by the desire to understand possible differences in our findings with those of Mahajan et al. (2023), which uses SHARP metadata to identify positions and fluxes of magnetic regions. The resulting amplitude and phase of the 11 yr variations are shown in Figure 14 and differ little from our nominal results obtained using our tabulated MRs. As noted earlier, differences between the distributions (Figure 3) are greatest within the lowest of our three flux groups, where SHARPs are sparse compared to the MRs used here. To understand this result, we isolated the contributions to the residuals in our nominal case expected from each of the three flux groups separately. We find that the medium and high-flux groups each contribute roughly 40% of the total amplitude while the low-flux group contributes only about 20% of the total amplitude. Thus, the excess numbers of MRs compared to SHARPs matter little to the final results.

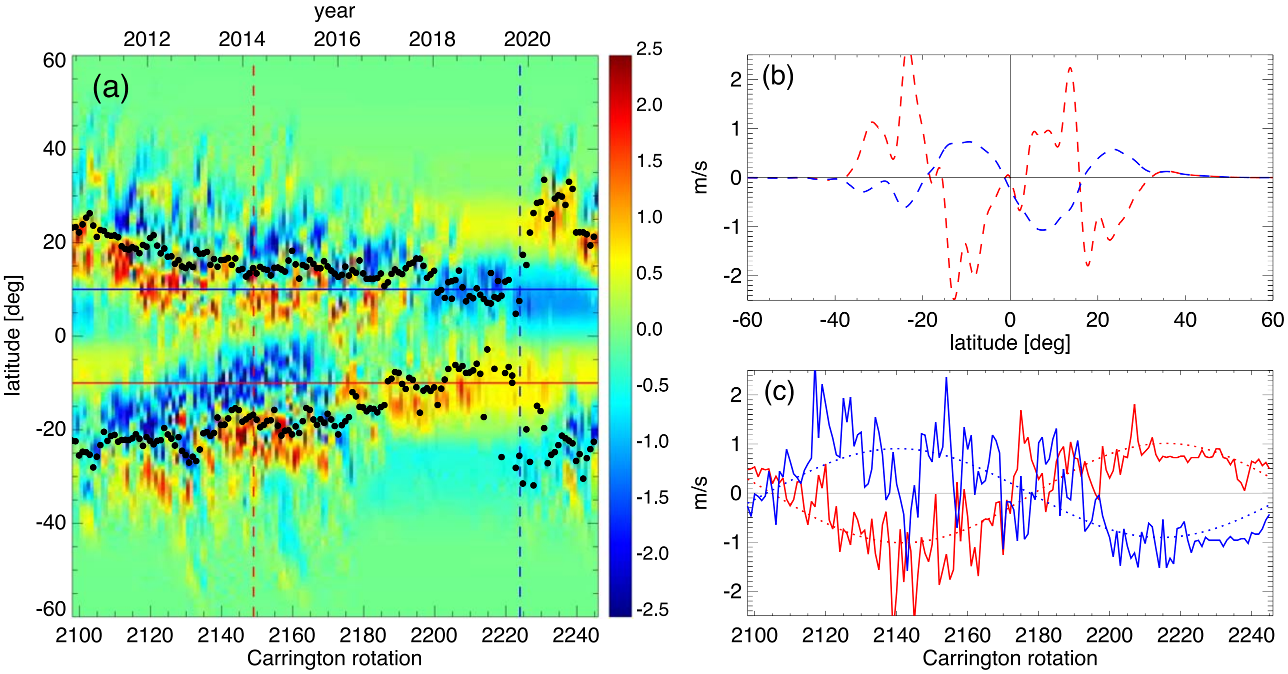

Figure 11. Meridional-flow residuals as estimated from individual MRs identified in this study. Panel (a) shows the residuals for each CR as a function of the date and latitude. Black circles indicate the mean latitudes of the MRs in either hemisphere over each CR. The dashed vertical lines in (a) indicate specific dates for which slices of the meridional residual as a function of the latitude are shown by lines of the same colors in panel (b). Likewise, the horizontal lines in (a) indicate specific latitudes (±10°) for which the time variations of the residuals are shown, using the same colors, in panel (c). The dotted lines in (c) show the fits to the observed variation with a sine function with a period of 11 yr.

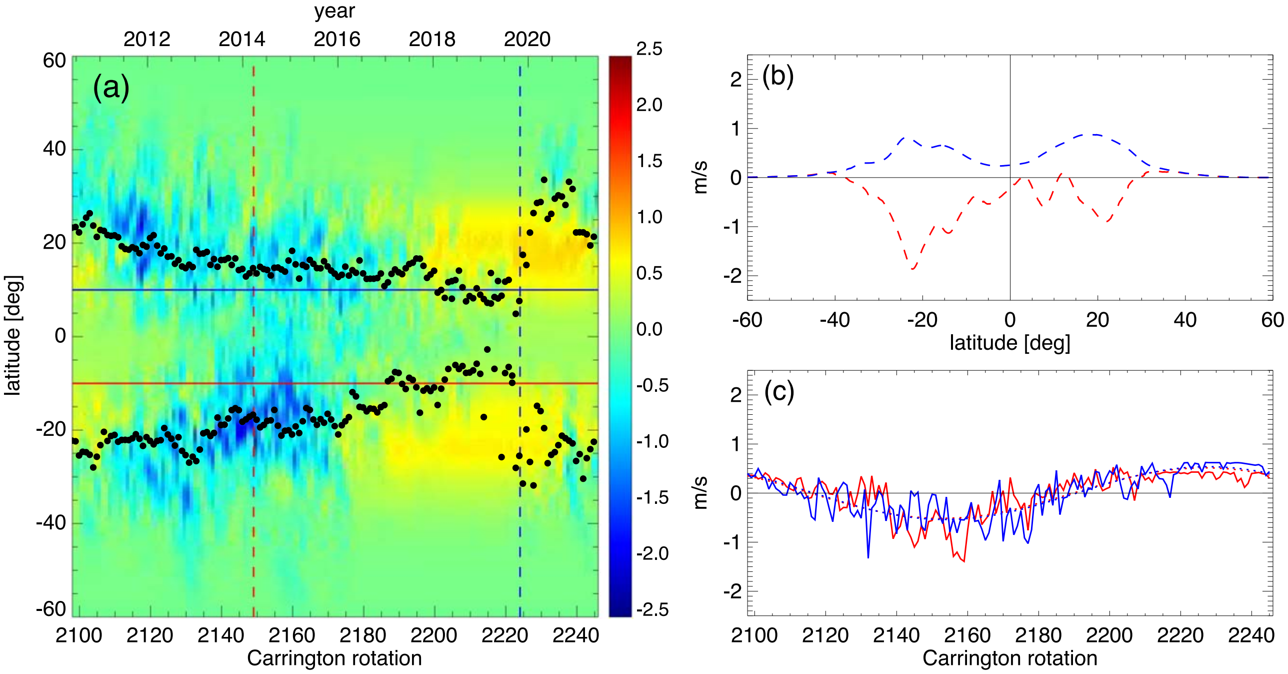

Figure 12. Zonal-flow residuals as estimated due to individual magnetic regions identified in this study. The format is identical to Figure 11. Note that the sine function fits in (c) are almost indistinguishable.

Additional estimates were made to test the sensitivity of the results to the threshold flux as well as to the details of how regions are partitioned into flux groups. The threshold flux $\Phi_{\text{thresh}} = 5 \times 10^{20}$ Mx, is established empirically and thus subject to uncertainty. Consequently, we examined how the results changed by either halving or doubling the flux threshold. Overall, allowing more or less "low" flux regions into the CR averages by changing this threshold produced changes in the amplitudes within active latitudes amounting to less than 10%. We note that Poulier et al. (2022) used a threshold flux of 10^{21} Mx, which is identical to the larger value tested. Our test provides evidence against this choice of cutoff flux as having a major impact on their findings, as was suggested by Mahajan et al. (2023).

Finally, we note that the amplitudes of sine-wave fits shown in the active latitudes in Figure 13 increase only modestly (by

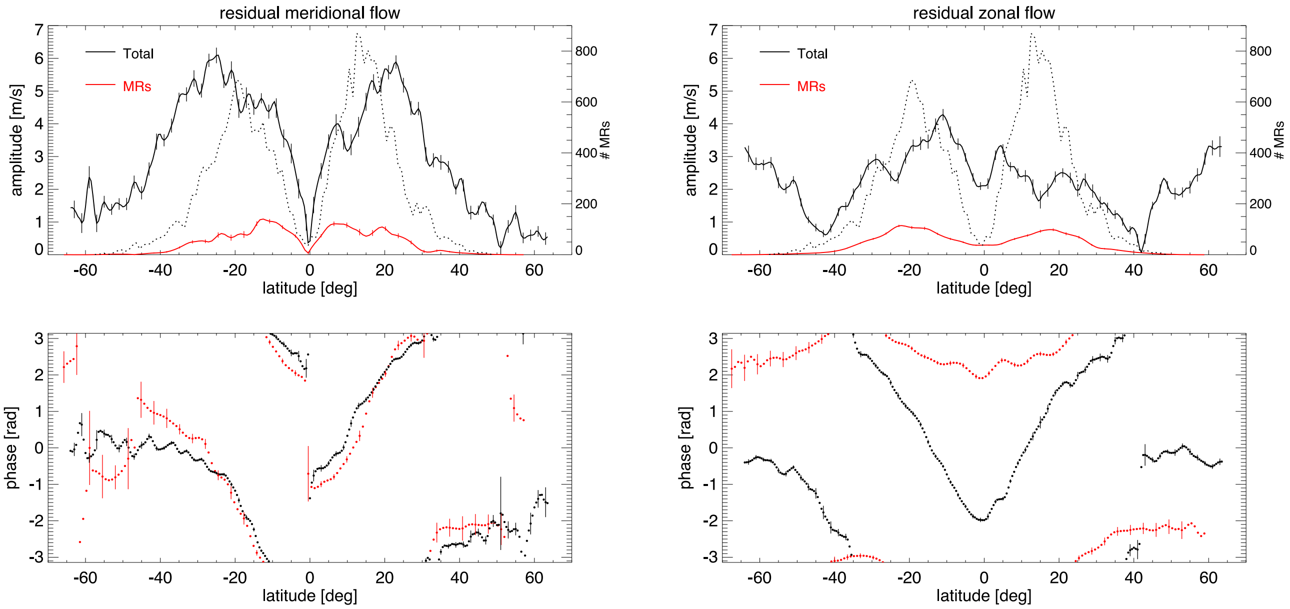

Figure 13. Amplitude (top panels) and phase (bottom panels) of temporal variations of flows in the meridional (left panels) and zonal (right panels) directions. In the top panels, black lines indicate the results for the total residual meridional flow while red lines indicate the contribution due to the magnetic regions identified in this study. The dotted lines show a histogram in latitude of all magnetic regions over the 11 yr interval as indicated by the scale on the right. In the bottom panels, black dots indicate results for the total residuals while red dots indicate the contribution due to magnetic regions. Only some error bars are shown for clarity.

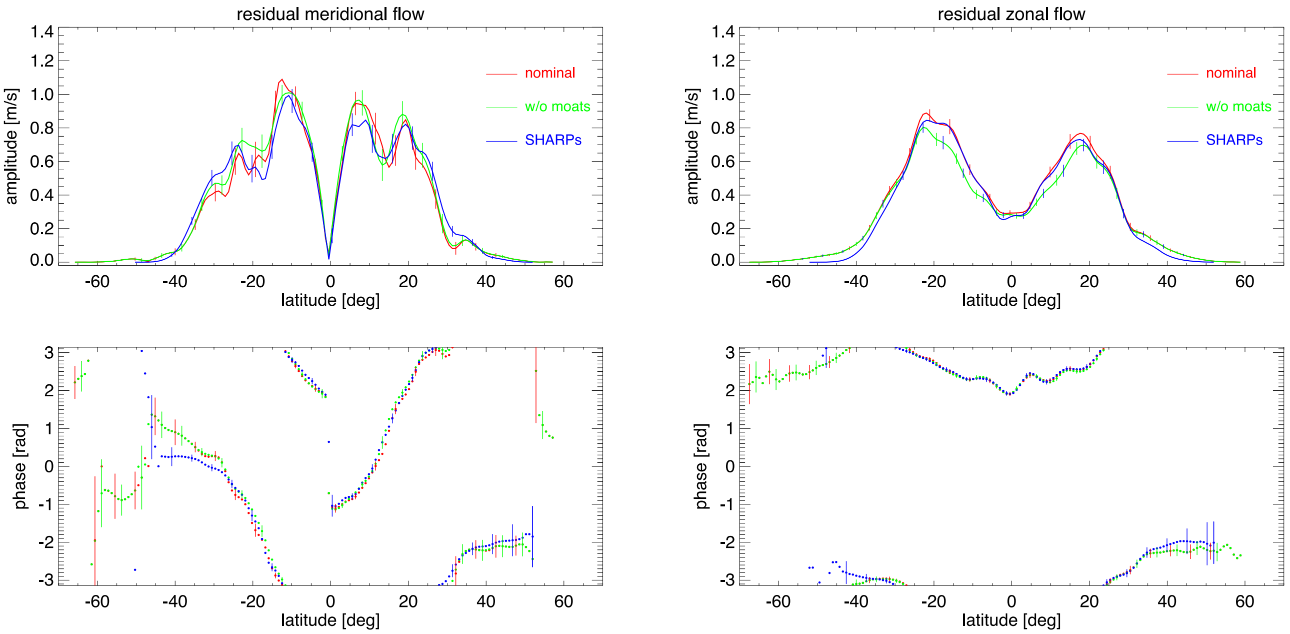

Figure 14. Amplitude and phase of temporal variations of flows contributed by magnetic regions in a format similar to Figure 13 showing results under different assumptions. Red lines (top panels) and circles (bottom panels) show the nominal results as shown in Figure 13. Results in green represent those obtained by excluding sunspot moats, while results in blue are based on substituting our MR tables with SHARP observations.

~30%) when all magnetic regions are assigned to the medium-flux group and assumed to have the corresponding flow profiles. This gives us some confidence that the large disparity between the total residual variations and those predicted by magnetic regions does not arise from fine details as to how the flux groups are partitioned.

6. Discussion

We have estimated the amplitude and phase of the solar cycle variation in the global meridional circulation and rotation rate due to local flows around all identified magnetic regions in an 11 yr interval. Our main findings are that local MR flows contribute, at most, about 1 m s^{-1} to the residuals of either component over a solar cycle. From studies of global flows in the near-surface (e.g., Zhao et al. 2014; Howe et al. 2018; Komm et al. 2020) the known amplitudes of these residuals are three to five times greater than this, implying that local magnetic regions are not the major source, in the active latitudes, of either the torsional oscillations or the 11 yr variation in the meridional circulation. Furthermore, the contributions expected from the relatively compact flows associated with magnetic regions largely disappear at latitudes higher than 40°, whereas 11 yr residuals continue to be observed at these latitudes.

To our knowledge, the measurements presented here include the first quantitative estimate of the contribution to the torsional oscillation due to magnetic region flows. In spite of the prediction of Spruit (2003), observed vortical flows near magnetic regions appear to be insufficient by a factor of several to produce the known amplitude of the torsional oscillation. Moreover, the latitude variation of the phase of the magnetic region contribution is not consistent with the properties of the torsional oscillation. Part of this failure arises from the asymmetric zonal-flow profiles near magnetic regions (see Figure 9). Magnetic regions tend to be flanked by retrograde motions on their poleward side (Braun 2019; Gottschling et al. 2021) with no noticeable prograde counterparts on their equatorward side. Specifics of local flows aside, the general findings here are consistent with a characterization of the torsional oscillation as a global phenomenon that persists to latitudes significantly higher than active regions (Howe 2009) and throughout much of the convection zone (Vorontsov et al. 2002).

The low amplitudes of the meridional residuals expected from magnetic regions are consistent with ring-diagram analyses, which have applied masks to flow measurements (González Hernández et al. 2008; Komm et al. 2020). Komm et al. (2020) find the amplitude of the solar cycle variation for the "active region" masked subset of the data to be 9% (33%) larger than the "quiet" subset for meridional (zonal) flows. These values represent fairly incremental contributions from the active subset. Mahajan et al. (2023) find evidence for inflows toward active regions, selected from SHARP metadata, which extend as far as 30° away from their centers. Consequently, Mahajan et al. (2023) suggest that the quiet subsets of the ring-diagram analysis, as well as the masks used by Poulier et al. (2022), may be contaminated with these extended flows. On the other hand, the inflows we observe here are found to be far more compact, mostly disappearing into noise at 10°–12° from their centers. Mahajan et al. (2023) also suggest that prior studies (Braun 2019; Poulier et al. 2022) may suffer from incomplete tabulations of magnetic regions. This issue of the completeness of our lists of magnetic regions is explored in Section 2. Our findings suggest a flux threshold that is a factor of 2 lower than those considered by Braun (2019) and Poulier et al. (2022), but the tests discussed in Section 5 indicate that the omission of these very low-flux MRs is unlikely to be the main cause of disparate results between Poulier et al. (2022) and Mahajan et al. (2023).

Understanding the differences between flow measurements made from different helioseismic and feature-tracking methods in the presence of nearby sunspots and regions of strong fields may be critical to fully resolving this issue. Artificial data, constructed using simulations of wave propagation and flows in the vicinity of magnetic fields (e.g., Rempel & Schlichenmaier 2011; DeGrave et al. 2014; Felipe et al. 2017), can be useful in providing target flows for these purposes.

Acknowledgments

We thank Hannah Schunker and the anonymous referee for helpful suggestions on drafts of this publication, and K.D. Leka for enlightening discussions on active regions. This work is supported by the NASA Heliophysics Division through its Living With a Star program (grant 80NSSC20K0187. Additional support is provided by the NASA Guest Investigator program (grant 80NSSC22K0754) and by the COFFIES DSC (Cooperative Agreement 80NSSC22M0162). Resources supporting this work were provided by the NASA High-End Computing (HEC) Program through the NASA Advanced Supercomputing (NAS) Division at Ames Research Center. SDO data are provided courtesy of NASA/SDO and the AIA, EVE, and HMI science teams.

Appendix

Magnetic Flux Definition as Compared with USFLUX

SHARPs denote magnetic regions automatically identified by algorithms developed by the SDO/HMI team as part of routine vector magnetic field observations (Hoeksema et al. 2014). SHARPs are not compiled until regions undergo an entire disk passage, and their inclusion is based on many criteria including their evolution during disk passage (Bobra et al. 2014). Included with the SHARP metadata is the value of USFLUX, which represents the unsigned flux within a patch, intended to isolate "active pixels", and which varies substantially over the evolution of the region.

We show in this appendix how USFLUX differs from the fixed-box flux measurements used here, which are the same as those used by Braun (2019) and Poulier et al. (2022). In particular, there are important distinctions between these flux measurements, which are relevant to comparisons of different methodologies (Mahajan et al. 2023).

Figure 15 shows the line-of-sight magnetic field in the vicinity of four SHARPs, selected to represent typical regions in the lowest quartile of their flux distribution. It is clear that the masks over which USFLUX is assessed contain only a fraction of the flux as present in the larger bounding box used both in this analysis and that of Braun (2019).

Figure 16 shows a scatter plot of USFLUX against the values of $\Phi_{\rm box}$ obtained with the bounding box used here. The two fluxes are similar for significantly strong regions, but it is clear that for the weakest regions, USFLUX can be an order of magnitude lower than the corresponding value of $\Phi_{\rm box}$. We also note that at higher fluxes, the use of our fixed bounding box may underestimate the total flux associated with the MR, since the strongest regions may exceed the boundaries. In spite of this shortcoming, we find this flux definition, measured over a fixed box, to be well suited for its primary use in separating the MRs into the three general groups as shown in Figure 3.

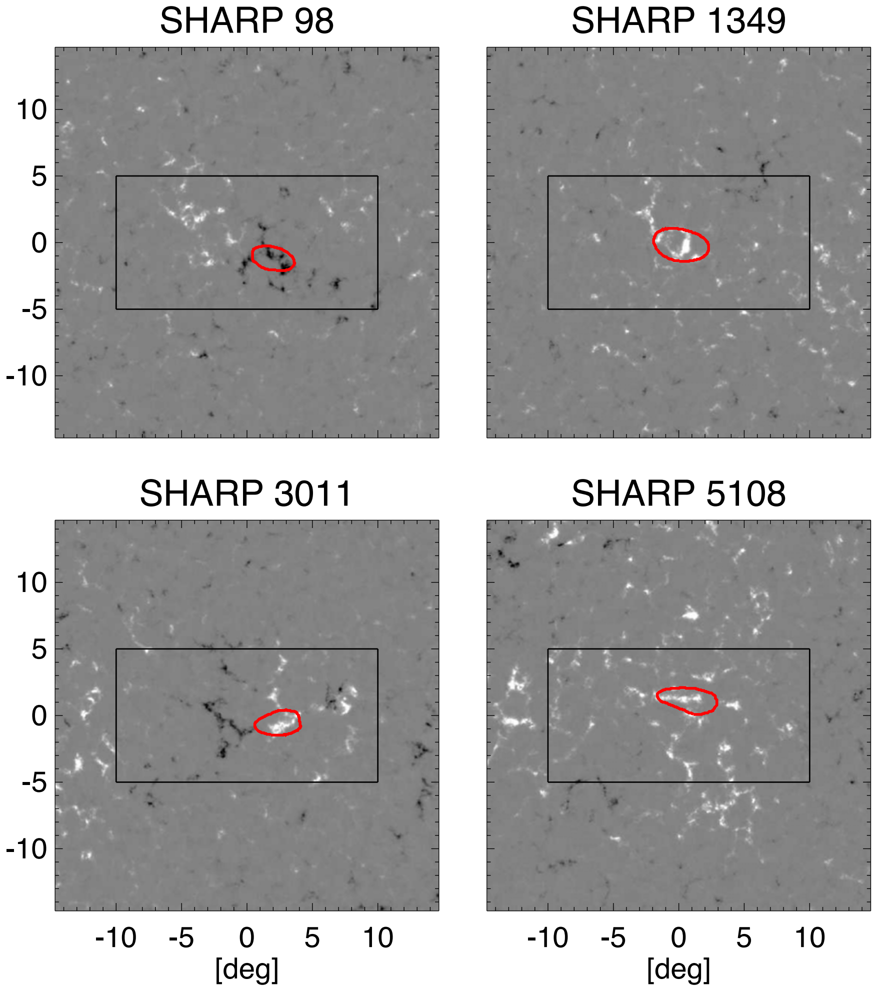

Figure 15. Line-of-sight magnetic flux density in the vicinity of four representative, low-flux, SHARP regions. The red curves indicate the region of active pixels over which the unsigned flux parameter, USFLUX, is computed. The rectangular box indicates the area over which the quantity Φ_{box} is measured. These quantities can differ by more than an order of magnitude.

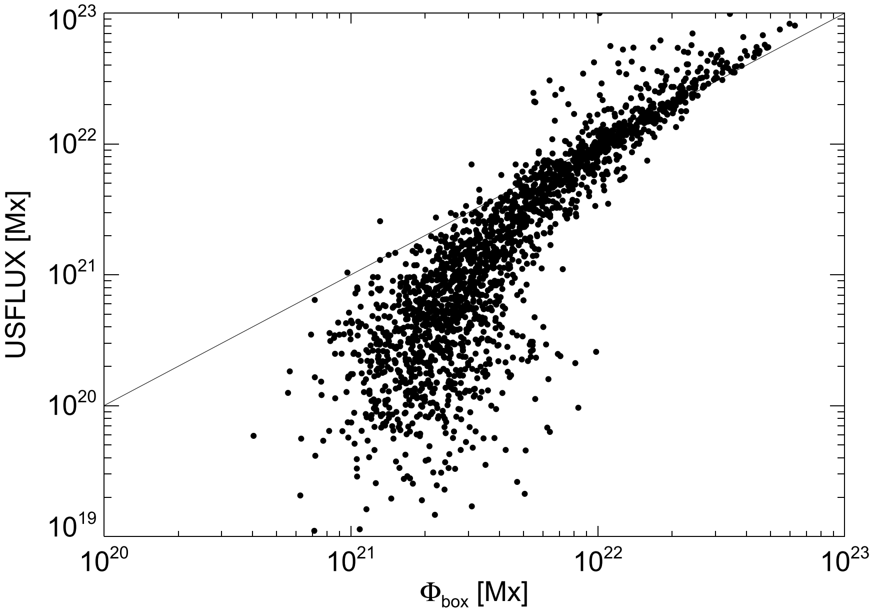

Figure 16. Scatter plot of USFLUX against Φ_{box} for the entire sample of SHARPs, measured daily. For clarity, only a random 10% of the points are shown. The solid line indicates a slope of unity.

ORCID iDs

D. C. Braun https://orcid.org/0000-0001-6840-2717

References

Basu, S., & Antia, H. M. 2003, ApJ, 585, 553
Beaudoin, P., Charbonneau, P., Racine, E., & Smolarkiewicz, P. K. 2013, SoPh, 282, 335
Bobra, M. G., Sun, X., Hoeksema, J. T., et al. 2014, SoPh, 289, 3549
Braun, D. C. 2016, ApJ, 819, 106
Braun, D. C. 2019, ApJ, 873, 94
Braun, D. C., & Wan, K. 2011, JPhCS, 271, 012007
Chou, D.-Y., & Dai, D.-C. 2001, ApJL, 559, L175
DeGrave, K., Jackiewicz, J., & Rempel, M. 2014, ApJ, 794, 18
Felipe, T., Braun, D. C., & Birch, A. C. 2017, A&A, 604, A126
Gizon, L., Cameron, R. H., Pourabdian, M., et al. 2020, Sci, 368, 1469
Gizon, L., Duvall, T. L., Jr., & Larsen, R. M. 2001, in IAU Symp. 203, Recent Insights into the Physics of the Sun and Heliosphere: Highlights from SOHO and Other Space Missions, ed. P. Brekke, B. Fleck, & J. B. Gurman (San Francisco, CA: ASP), 189
González Hernández, I., Howe, R., Komm, R., & Hill, F. 2010, ApJL, 713, L16
González Hernández, I., Kholikov, S., Hill, F., Howe, R., & Komm, R. 2008, SoPh, 252, 235
González Hernández, I., Komm, R., Hill, F., et al. 2006, ApJ, 638, 576
Gottschling, N., Schunker, H., Birch, A. C., Löptien, B., & Gizon, L. 2021, A&A, 652, A148
Haber, D. A., Hindman, B. W., Toomre, J., & Thompson, M. J. 2004, SoPh, 220, 371
Hanasoge, S. M. 2022, LRSP, 19, 3
Harvey, K. L., Harvey, J. W., & Martin, S. F. 1975, SoPh, 40, 87
Hathaway, D. H., & Rightmire, L. 2010, Sci, 327, 1350
Hathaway, D. H., Upton, L. A., & Mahajan, S. S. 2022, FrASS, 9, 419
Hindman, B. W., Haber, D. A., & Toomre, J. 2009, ApJ, 698, 1749
Hoeksema, J. T., Liu, Y., Hayashi, K., et al. 2014, SoPh, 289, 3483
Hotta, H., Bekki, Y., Gizon, L., Noraz, Q., & Rast, M. 2023, SSRv, 219, 77
Howard, R., & LaBonte, B. J. 1980, ApJL, 239, L33
Howe, R. 2009, LRSP, 6, 1
Howe, R., Christensen-Dalsgaard, J., Hill, F., et al. 2005, ApJ, 634, 1405
Howe, R., Hill, F., Komm, R., et al. 2018, ApJL, 862, L5
Komm, R., Corbard, T., Durney, B. R., et al. 2004, ApJ, 605, 554
Komm, R., Howe, R., & Hill, F. 2018, SoPh, 293, 145
Komm, R., Howe, R., & Hill, F. 2020, SoPh, 295, 47
Lindsey, C., & Braun, D. C. 2004, ApJS, 155, 209
Löptien, B., Birch, A. C., Duvall, T. L., et al. 2017, A&A, 606, A28
Mahajan, S. S., Sun, X., & Zhao, J. 2023, ApJ, 950, 63
Martin, S. F., & Harvey, K. H. 1979, SoPh, 64, 93
Pipin, V. V., & Kosovichev, A. G. 2019, ApJ, 887, 215
Poulier, P. L., Liang, Z. C., Fournier, D., & Gizon, L. 2022, A&A, 664, A189
Rempel, M. 2006, ApJ, 647, 662
Rempel, M., & Schlichenmaier, R. 2011, LRSP, 8, 3
Rightmire-Upton, L., Hathaway, D. H., & Kosak, K. 2012, ApJL, 761, L14
Scherrer, P. H., Bogart, R. S., Bush, R. I., et al. 1995, SoPh, 162, 129
Scherrer, P. H., Schou, J., Bush, R. I., et al. 2012, SoPh, 275, 207
Schou, J., Scherrer, P. H., Bush, R. I., et al. 2012, SoPh, 275, 229
Spruit, H. C. 2003, SoPh, 213, 1
Ulrich, R. K. 2010, ApJ, 725, 658
van Driel-Gesztelyi, L., & Green, L. M. 2015, LRSP, 12, 1
Vorontsov, S. V., Christensen-Dalsgaard, J., Schou, J., Strakhov, V. N., & Thompson, M. J. 2002, Sci, 296, 101
Zhao, J., Couvidat, S., Bogart, R. S., et al. 2012, SoPh, 275, 375
Zhao, J., & Kosovichev, A. G. 2004, ApJ, 603, 776
Zhao, J., Kosovichev, A. G., & Bogart, R. S. 2014, ApJL, 789, L7